

Stable, Scalable Micron-Sized Porous Silicon for High Energy Density Li-Ion Batteries

Akam Osmanpour, Jurgen Poen, Vanesa Ruiz, Kamran Tariq, and Willem Peter Kalisvaart*

Metallurgical-grade silicon is a low-cost, high-capacity alternative material for Li-ion battery anodes. Herein, a unique, low specific surface area (SSA) porous silicon with highly regular, parallel, internal pore structure is presented. The relatively low SSA results in a first cycle Coulombic efficiency of over 90% in a half-cell configuration. Balancing (full) cells with high-nickel content cathode material at a limited Si specific capacity around 1000 mAh g⁻¹ limits stack expansion to under 4% in a multilayer pouch cell configuration (consisting of double-sided coated anodes and cathode foils). This limited expansion is ascribed to the persistence

of a crystalline Si backbone, directing most of the expansion inwards. This mechanism is confirmed by cross-sectional scanning electron microscopy on a lithiated anode and Raman microscopy on a cycled electrode. After 100 cycles, just under 50% of the original amount of c-Si is still present, as detected by X-ray diffraction. For the optimum electrode formulation and particle size distribution (PSD), full cells using NMC622 cathodes last more than 200 cycles before falling below 80% state-of-health, and the porous Si powder significantly outperforms a nonporous powder with a similar PSD.

1. Introduction

Silicon has by far the highest specific storage capacity for Li among all group 14 and 15 elements (3579 mAh g⁻¹), alloying up to 3.75 Li atoms per host atom. The main disadvantage of any ultrahigh-capacity anode material is the extreme volume changes upon full lithiation/delithiation; 270% in the case of silicon.^[1–3] Major cell manufacturers have stated their intent to use minor amounts of (nanosized) silicon or SiO_x blended with graphite anodes to boost the capacity.^[4] Examples where small amounts (<10 wt.%) of Si or SiO_x is present in cylindrical cells relate to Murata,^[5] Samsung or LG,^[6] or pouch cells, such as cells produced by Envia/Zenlabs,^[7] etc.

Nanosized elemental silicon is usually made using silane gas (SiH₄)^[8,9] which is highly toxic and flammable. Furthermore, the high specific surface area (SSA) of nanosized materials leads to large amounts of electrolyte decomposition and lower first-cycle efficiency, drastically reducing the specific energy that can be reached in a cell.^[10] On the contrary, nanostructured, porous silicon with a relatively large secondary particle size, has also been extensively studied as an attempt to retain high capacity and improve cycling stability. The Si-Al eutectic composition is often used as a starting point for generating high porosity, since Al is

quite reactive and easy to etch. However, this particular composition has quite low Si content^[11,12] (12%), and the resulting structure is not very mechanically robust as a result. Another popular method is magnesiothermic reduction of porous SiO₂, but these preparation methods for porous Si usually result in high SSAs, leading to high irreversible losses in the first charge-discharge cycle.^[13–15] What a priori can be anticipated as favorable is a material combining improved electrolyte access with mechanical robustness and relatively low (<10 m² g⁻¹) SSA.

Metallurgical grade, micron-scale silicon^[1,16–18] has a number of advantages as a high-capacity anode material for Li-ion batteries: 1) low price compared to chemical vapour deposition grown Si, (and about 1/3 that of graphite^[19]), and high abundance; 2) avoids supply and export restrictions on battery-grade graphite; 3) easiness of transport as opposed to transport of SiH₄; and 4) low surface area. The last point in particular is relevant since high surface area, for example, in electrodes using nanosized silicon, leads to high first cycle losses through electrolyte decomposition, which increases impedance and reduces the amount of mobile lithium in the cell. On the contrary, larger particle size makes the material more prone to fracture upon lithiation, as the material expands by ≈75% for every 1000 mAh g⁻¹ worth of Li that is alloyed with Si.^[20] In order to mitigate outward expansion and fracture, cells can be balanced to utilize only up to ≈1000–2000 mAh g_{Si}⁻¹ of Si, above which the marginal gains in energy density for every mAh g⁻¹ increase in Si utilization rapidly decrease.^[21] In addition, internal structure, such as porosity, can be introduced to direct the expansion of Si inwards rather than outwards.^[22] By properly balancing the cell at ≈1000–2000 mAh g_{Si}⁻¹, part of the material remains as a rigid, crystalline backbone, thus directing a large part of the material expansion toward the particle interior, as shown in **Scheme 1** for an idealized material.

Herein, we present an elaborate characterization and cycling study on E-magy porous Si, which has an internal structure strongly

A. Osmanpour, J. Poen, V. Ruiz, K. Tariq, W. P. Kalisvaart

Battery Qualification Department

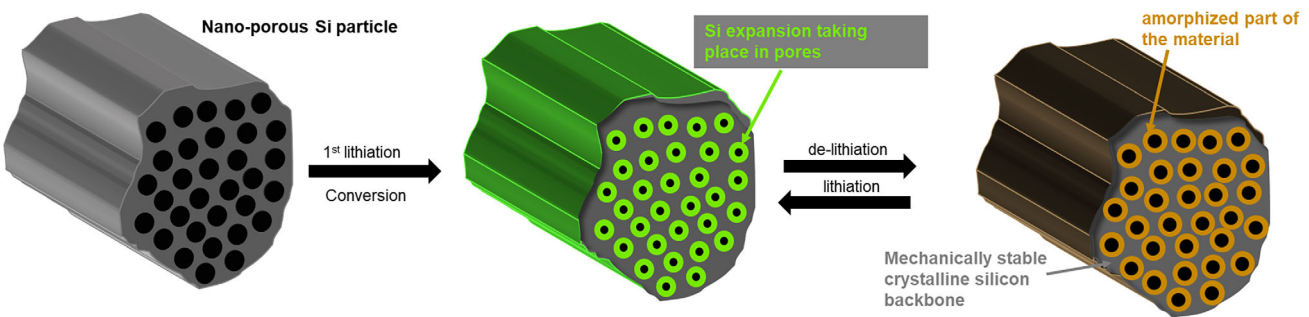
E-magy

Bijlestaal 54A, Broek op Langedijk 1721 PW, The Netherlands

E-mail: peter.kalisvaart@e-magy.com

Supporting information for this article is available on the WWW under <https://doi.org/10.1002/batt.202500500>

© 2025 The Author(s). *Batteries & Supercaps* published by Wiley-VCH GmbH. This is an open access article under the terms of the Creative Commons Attribution-NonCommercial License, which permits use, distribution and reproduction in any medium, provided the original work is properly cited and is not used for commercial purposes.

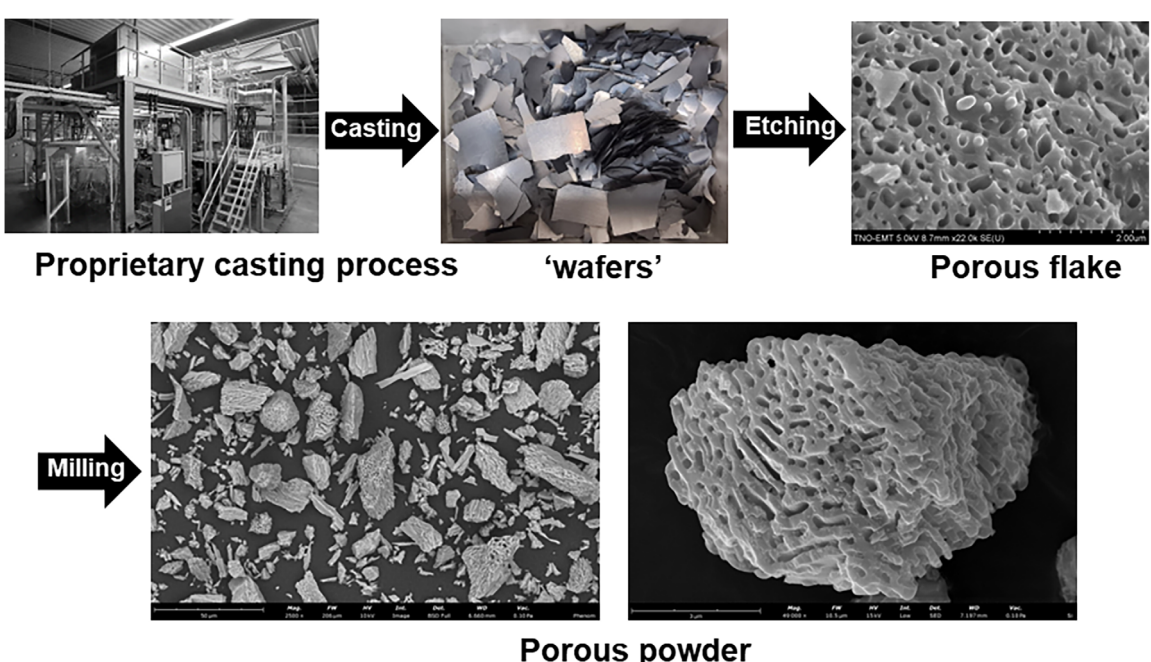


Scheme 1. Illustration that represents the amount of Si material that undergoes amorphization, where the green areas represent the expanded area, the orange areas represent the amorphous Si, and the gray areas represent the rigid crystalline Si.

resembling the idealized picture from Scheme 1 with cylindrical, parallel pores. In the first lithiation/conversion step, a certain amount of material is amorphized within the volume of the pores (as depicted by the light green color). The reaction mechanism is studied in detail using direct observation by electron microscopy and areal mapping of crystalline silicon using Raman microscopy. Also, we evaluated and quantified the remaining crystalline-Si using X-ray diffraction (XRD). Experimental results largely confirm the mechanism depicted in Scheme 1. Micron-sized, porous Si (E-magy) is shown to have superior performance to nonporous Si with similar particle size distribution (PSD), both in terms of electrode expansion and capacity retention.

melt of silicon and a transition metal produced “wafers” with a two-phase structure of elemental Si and a transition metal-disilicide phase ($TMSi_2$). After an etching step, structured porosity was formed in the material. Etching was carried out in an aqueous HF solution of up to 20 wt%. The concentration was gradually increased during the process to avoid excessive heating and hydrogen formation. After etching, the flakes were washed with isopropanol to avoid excessive surface oxidation during drying, which would occur if water were used. More surface oxide also reduced the initial Coulombic efficiency (CE) and could reduce cycle life.

The material will already partially break up during the etching step. Using either planetary ball-milling (Retsch PM 100) or jet-milling (Hosokawa Alpine), the fragmented porous flakes were subsequently processed into a finer powder. The two scanning electron microscopy (SEM) micrographs at the bottom of Scheme 2, obtained with a Phenom Pharas G2 Desktop FEG-SEM, show the regular pore structure inside the particles. More detailed descriptions of the casting, etching, and milling process can be found in the patent literature.^[23,24]



Scheme 2. Summary of E-magy's powder preparation process (SEM images Courtesy of ThermoFisher Scientific).

After fully etching the TiSi_2 phase, the resulting porosity of the flakes should be ≈ 32 vol%, based on the composition of the melt, the molar volume of the TiSi_2 phase, and the weight loss during etching. Mercury intrusion porosimetry was performed by Delft Solid Solutions according to ISO 15,901–1:2016 on porous flakes (see Scheme 2, top right). The measured porosity was equal to the theoretical value within experimental error as shown in Figure S1, Supporting Information. The SSA of the powder is typically $4\text{--}5 \text{ m}^2 \text{ g}^{-1}$ as determined by Brunauer–Emmet–Teller (BET) (N_2 -gas adsorption). Some variations of silicon materials having different PSDs were compared in this work, exhibiting different amounts of fines and overall features. PSD_1 and PSD_2 refer to ball-milled and jet-milled powders, respectively, having a certain contribution of fines (around $<1 \mu\text{m}$). PSD_3 was produced by using an elbow classifier in order to remove fines in the material.^[25] This material is referred to as ‘all-porous’ Si material. A fourth sample, PSD_4, was produced by ball-milling and sedimentation, to partially remove fines, and was reproduced in nonporous form for comparative purposes (referred to as nonporous PSD_4). The powder characteristics are listed in Table S1, Supporting Information.

2.2. Electrode Formulation and Anode Casting

Silicon anodes were made with 80–85 wt% Si, 5–10 wt% carbon additives, and 10 wt% of partially neutralized (up to 2/3rd) polyacrylic acid (Sigma Aldrich, Mw = 450,000). Lithium hydroxide (LiOH) was used for neutralization (in a 10% water-based solution). Carbon additives are a mixture of mainly KS6 flake graphite, SC45 or a Carbon Black from Cabot’s ‘LITX’ series, and up to 0.25 wt% of single-wall carbon nanotubes (SWCNTs, Betterial). Components were mixed in a centrifugal mixer (Thinky Are-250) at 1500–2000 rpm and added to the neutralized binder solution in order of increasing particle size: SWCNTs first, Si powder last. The slurry was then coated onto a 10 μm Cu foil and dried for 1 h at 80 °C. Electrodes were cut to 12.7 mm (1/2 in.) diameter discs for electrochemical testing. Before cell assembly, both anode and cathode are dried again at 80 °C overnight under vacuum.

2.3. Cell Assembly and Testing

Cycling was done using 2032 coin cells made of 304 stainless steel from Seika. The electrolyte was 1 M LiPF_6 in EC:EMC (3:7 w/w) with 10 wt% FEC additive purchased from E-lyte. One sheet of Celgard 2500 (19 mm dia.) and one glass fiber disk (15 mm dia., 0.26 mm thick before compression) were used as separators. Electrolyte dosage for coin cells was 45 μl onto the glass fiber disk. Half-cells were cycled at a depth of 1000 $\text{mAh g}_{\text{Si}}^{-1}$ with 0.25 mm thick Li foils (AOT) as counter-electrodes. The upper voltage cutoff was 1.0 V versus Li metal. Full cells were balanced around 1000 $\text{mAh g}_{\text{Si}}^{-1}$ $\pm 10\%$ in a voltage range of 3–4 V using NMC622 cathode material from CustomCells or NMC83 material from BASF. The areal loading of active Si was 1.5–1.7 mg cm^{-2} . The nominal capacity of the cathode sheets (3–4.2 V vs. Li metal) was 2 mAh cm^{-2} . The full-cell voltage range was limited to 3–4 V in order to not stress the cathode material and ensure capacity degradation was mostly due to the Si anodes being studied. Formation was conducted at

C-rates of 0.1 C (2 cycles) and 0.2 C (2 cycles), after which duty cycling was performed at 0.5 C. Cycle life was defined as the number of cycles until the cell discharge capacity declined to less than 80% of that in the fifth cycle (immediately after formation).

3-layer (single-sided coated anodes and cathodes) pouch cells were also assembled (via manual stacking). The dimension of the cathode layers being 6 \times 4 cm. Analogous cathode and electrolyte (1.5 ml) were used as for coin cells. The main difference in the cycling strategy is that pouch cells are degassed after formation to remove the gases generated in the process. Cycling of pouch cells was carried out with in-house-built clamps to ensure homogeneous pressure distribution (3 bar).

Battery cyclers from Neware were used for both coin cell (BTS-4000) and pouch cell (WIHW-200) testing within climatic chambers, maintaining a constant temperature of 25 °C during cycling.

2.4. Material Characterization

PSD of the silicon powder material was determined using laser diffraction (Horiba LA-350). SSA was determined by nitrogen adsorption (BET) measurements, performed on a Nova 600 physisorption analyzer (Anton Paar) using 11-point linearization between 50 and 300 mbar.

Anode expansion was characterized using an EL-CELL ECD-4-nano dilatometry setup at 25 °C.^[26] Half-cell configuration was used where silicon anode was tested against lithium metal. After a stabilization period of 24 h, the anode thickness was recorded during cycling at a specific current of 100 mA g^{-1} with regard to the silicon content in the anode. A 100% porous powder (PSD-3) and a nonporous powder are compared during a single lithiation up to 2000 $\text{mAh g}_{\text{Si}}^{-1}$.

Ex situ ‘rebound’ measurements were done using a Mitutoyo micrometer or contact gauge, both with a readability of 1 micrometre to measure the thickness before and after lithiation to the desired level. Operando stack expansion on a multilayer pouch cell was done using a similar method to Maroni et al.^[27] at a stack pressure of 2 bar.

XRD measurements were performed at INSA-Rennes on a Bruker D2 Phaser diffractometer using $\text{Cu K}\alpha$ radiation. Data was collected over a 2θ range between 10° and 60° in steps of 0.2°.

Lithiated anodes were ion-polished on a ThermoFisher CleanMill Ar ion mill polisher. SEM micrographs were obtained on a TESCAN Apreo 2 Field Emission SEM at 2 kV, also at ThermoFisher. Pristine or delithiated anodes were polished on a Hitachi IM4000 and imaged on a Hitachi S3700N SEM.

Raman Microscopy was performed on a Renishaw InVia confocal Raman microscope using a 633 nm laser. Step size was 0.25 μm and the exposure time was 2 s per spectrum recorded over a range between 200 and 800 cm^{-1} .

3. Results and Discussion

3.1. Reaction Mechanism

An ion milled cross-section of an electrode made with E-magy porous Si that had been lithiated up to 1000 $\text{mAh g}_{\text{Si}}^{-1}$ is shown

in Figure 1. Transfer between the coin cell battery and the ion mill, and subsequently, the ion mill and the SEM, was done entirely under inert atmosphere using the CleanConnect tool set.^[28] Top part of the image corresponds to the Cu substrate of the anode.

The SEM image in Figure 1 clearly shows that the inside of the pores is lithiated (denoted by the dark gray regions in the interior of the pores). This validates that the electrolyte has full access to all parts of the material, showing that the general reaction mechanism depicted in Scheme 1 is accurate. The outer surfaces of the particles also get visibly lithiated (note darker gray contour), a feature that was omitted for clarity in Scheme 1. The lighter gray areas in the particles corroborate that a significant part of the material remains crystalline.

The image contains numerous particles that exhibit no internal porosity. When the microstructure is relatively coarse, particles that are up to several microns in size can be formed without internal structure, but the zone where this happens is usually quite narrow, as shown in Figure S2, Supporting Information. Typically, 50%–70% of the material has pores that are smaller than 500 nm in diameter in both lateral axes (in case of elliptical pores).

Upon lithiation, crystalline Si (c-Si) gets transformed into amorphous Li_xSi where "x" = ~3. After delithiation, the Si remains amorphous, even when there is no more Li present. Therefore, the parts of the material that have been "activated", will have become amorphous, whereas the parts that serve as the rigid "backbone" will have remained crystalline. Both crystalline and amorphous silicon have a distinct Raman signature. Whereas, c-Si has a sharp peak around a shift of 520 cm⁻¹, amorphous Si has a broad band centered around 460 cm⁻¹ (see Figure S3, Supporting Information for example). These features can be mapped over an ion-polished area of a few-times cycled electrode in order to detect the amorphized areas of the material.

Raman mappings of two electrodes, one prepared with nonporous Si, and one with E-magy porous Si, are shown in Figure 2. The large particle on the left of the scanned area of the nonporous sample (Figure 2 top, selected area with a white square) has a crystalline core surrounded by an amorphized shell. For the

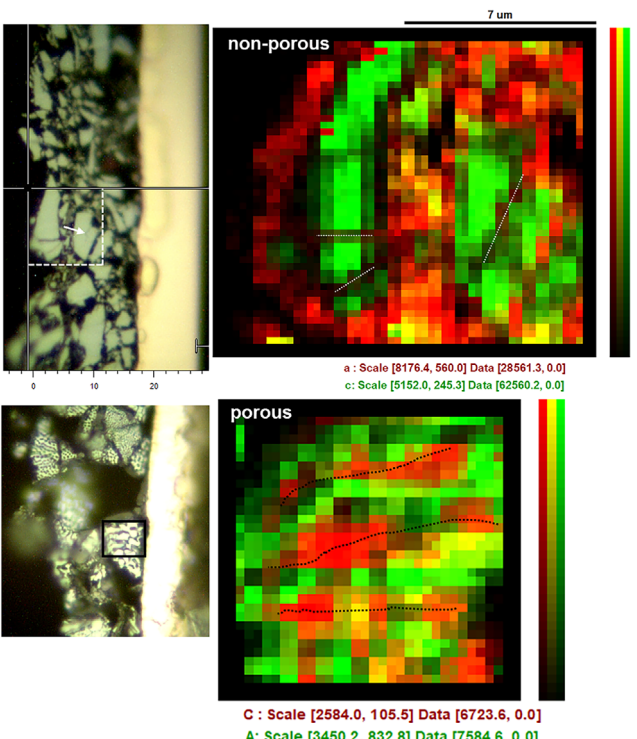


Figure 2. Raman mapping. Left: Optical (100x magnification) microscopy images of ion-polished cross-sections of electrodes with nonporous (top) and E-magy porous silicon (bottom) after three lithiation-delithiation cycles (half-cell); 'A' = amorphous, 'C' = crystalline. Scanned areas are marked by the dashed white and solid black squares. Fractures in the large nonporous particles are highlighted by white dotted lines.

porous particle in the lower part of Figure 2 bottom, crystalline and amorphous areas appear more stratified along the (coarse) pore structure in the scanned area of the particle (notice selected area with a black square).

Now we look at the electrochemical characterization of the Si anode materials. The initial CE for a half-cell is typically around 90%. Two loss mechanisms are considered: 1) electrolyte decomposition by reduction of solvent molecules, and 2) Li trapping

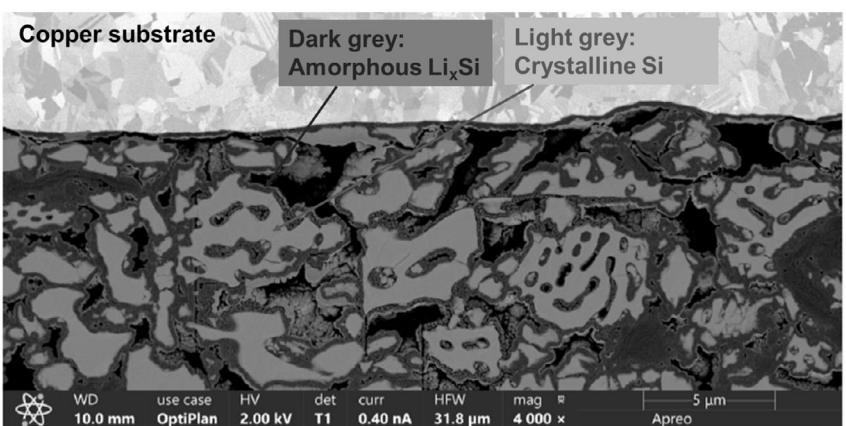


Figure 1. Ion-milled cross-section of an electrode prepared with PSD_2 powder (see Figure 3) lithiated to 1000 mAh g_{Si}⁻¹. The top part of the cross-section corresponds to Cu substrate. Courtesy of Thermo Fisher Scientific.

inside Si as we work within set voltage limits (1 V upper cutoff) and at a fixed current rate. In a half-cell configuration, the same amount (1000 mAh g⁻¹) of Li is added in each lithiation half-cycle, so Li trapping in the previous cycle will cause an equivalent amount of new c-Si to become activated in the next cycle, provided the loss associated with electrolyte decomposition remains the same.

Lithiation of c-Si and a-Si also have their own, and quite different, voltage characteristics. Thermodynamically, c-Si starts to lithiate below 0.15 V versus Li/Li⁺ and transforms to Li_xSi where $x \sim 3$. The voltage profiles in Figure S4, Supporting Information, show the typical behavior for c-Si in the first cycle, where the long flat plateau is typically seen at a half cell voltage between 0.09 and 0.12 V for E-magy silicon at a specific current of 100 mA g⁻¹. In the second cycle, more c-Si is being activated as there is again an almost flat part at the end of the lithiation. By the fifth cycle, this feature has nearly disappeared.

The 2 silicon materials having different PSDs compared in this work differ mainly in the amount of ultrafine material around 150 nm, SSA, as well as the amount of oxygen, as summarized in Table 1. For PSD_1, the anode formulation contained 80 wt% Si and no CNTs, whereas for PSD_2, the amount of Si was 85 wt% and the formulation also included 0.25 wt% SWCNTs. The CE profiles do look quite different between the two (Figure 3a). The first CE for PSD_1 is considerably lower than for PSD_2, which can be linked to its higher surface area. At the third cycle, the specific current is increased from 100 to 500 mA g⁻¹. PSD_1 shows a considerable decrease in CE at that point which is not seen for PSD_2. Also, in subsequent cycles, the CE is consistently lower for PSD_1 and only after ~ 30 cycles have both formulations stabilized. A different way to visualize this is by plotting the accumulated irreversible losses, as done in Figure 3b. Most of the difference is built up in cycle 1–30; after that, the small difference in CE in Figure 3a shows up as a slightly higher slope for PSD_1 in Figure 3b.

The amount of remaining c-Si over the course of cycling was monitored with XRD as shown above in Figure 3c. The relative integrated intensity (pristine/0 cycles' = 1) of the Si (111) peak with duplications (same anode sheet and cycling protocol, several months apart) is shown at various cycles 1, 2, 10, and 20, for PSD_1. The relative amount of c-Si is consistently, significantly higher for PSD_2 compared to PSD_1, but both stabilize after roughly the same number of cycles as the CE. Apparently, once the CE has stabilized, the main loss mechanism is electrolyte decomposition and not Li trapping.

Mechanistic information can, in principle, be derived from electrode voltage profiles and their dQ/dV curves derived from it.

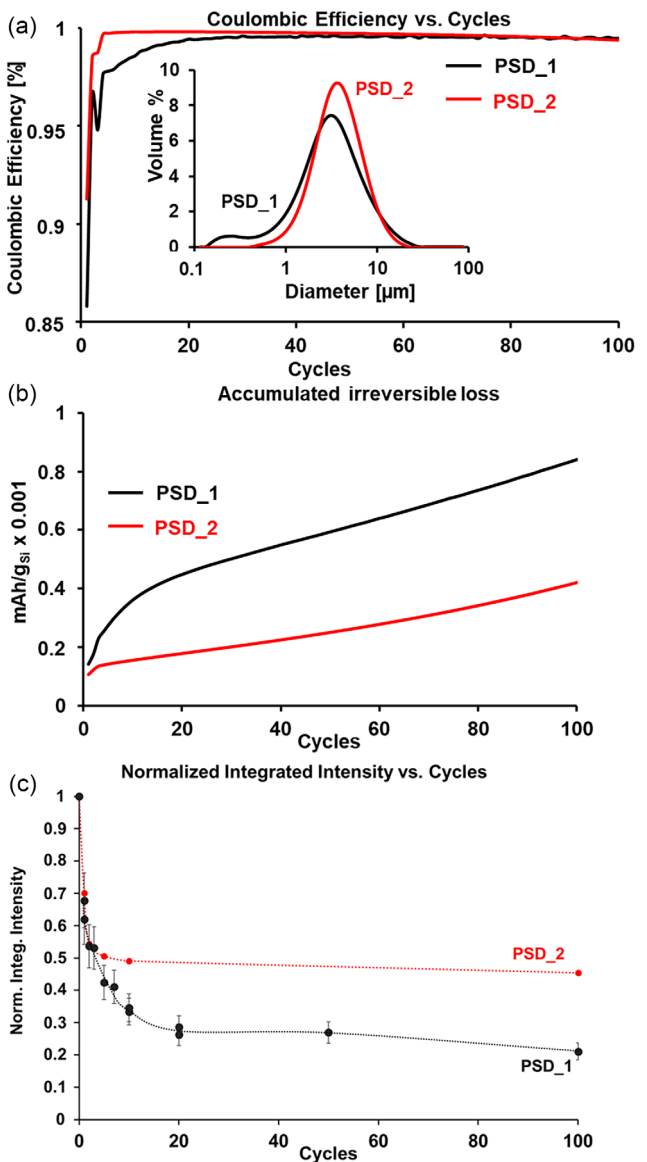


Figure 3. a) CE profiles of half-cells prepared with two different PSDs (PSD_1, PSD_2), b) accumulated irreversible capacity, and c) remaining fraction of crystalline silicon relative to the pristine electrode versus cycle number for both PSDs Si materials.

"dQ/dV" is the reciprocal of the derivative of the voltage profile; $1/(dV/dQ)$, and as a consequence, a plateau in the voltage profile becomes a peak in a dQ/dV curve. The aforementioned long lithiation plateau of c-Si becomes a sharp peak of almost infinite height in dQ/dV, as shown in Figure 4 for PSD_1 (top) and PSD_2 (bottom).

Table 1. Summary of powder properties for PSD_1 and PSD_2 powder.

	D10 ^{b)}	D50 ^{c)}	D90 ^{d)}	%O	SSA ^{e)}	1st CE ^{f)}
PSD_1 ^{a)}	0.90	2.85	7.55	3.6 [wt%]	14.3 [m ² g ⁻¹]	85.8 [%]
PSD_2	1.60	3.45	7.35	0.46 [wt%]	5.1 [m ² g ⁻¹]	91.2 [%]

^{a)}PSD: Particle Size Distribution; ^{b)}D10: particle size below which 10% of the particles in the sample fall; ^{c)}D50: median particle size; ^{d)}D90: the particle size below which 90% of the particles in the sample fall; ^{e)}SSA: Specific Surface Area; ^{f)}CE: Coulombic Efficiency.

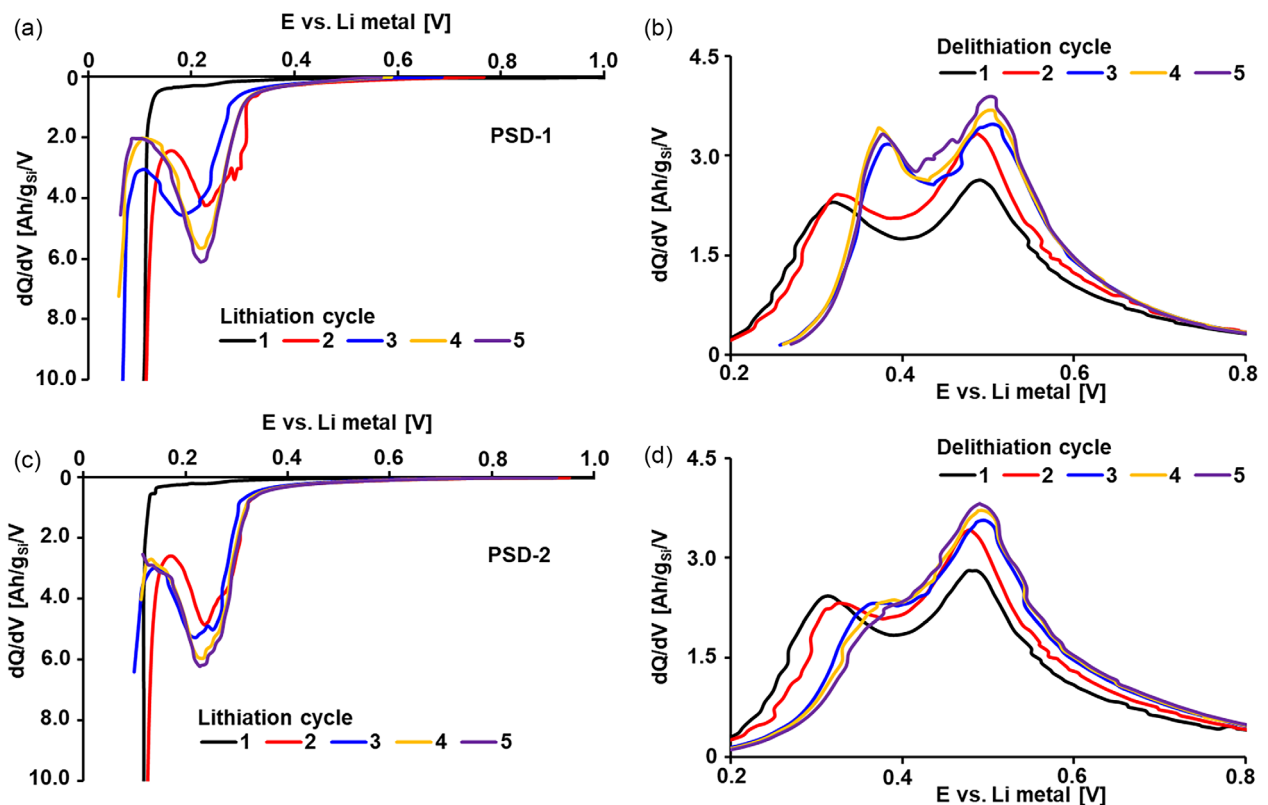


Figure 4. a) dQ/dV profiles for lithiation cycle 1–5 for an anode with PSD_1 powder, b) same as (a) for delithiation, c) lithiation dQ/dV profiles for an anode with PSD_2 powder, and d) same as (c) for delithiation. Note that going from cycle 2 to 3, the rate is increased from 100 to 500 mA g_{Si}⁻¹, causing a shift in the (de)lithiation voltage.

The sharp lithiation feature characteristic for c-Si at 0.1 V versus Li and below diminishes much more quickly for PSD_2 compared to PSD_1, indicating that considerably less additional c-Si is being activated per cycle for PSD_2. This is in line with the information extracted from XRD.

The delithiation dQ/dV profiles for PSD_1 (Figure 4b) show a more prominent peak at ≈ 0.35 V compared to PSD_2 (Figure 4d). The overall shape of the dQ/dV profiles in cycle 3–5 still strongly resembles that of the 1st cycle for PSD_1, showing that a larger/sharper peak at 0.35 V correlates with a more prominent lithiation dQ/dV feature below 0.1 V (compare Figure 4a,c and, therefore, with activation of additional c-Si in the preceding lithiation. The dQ/dV data are, therefore, consistent with the XRD data, which also showed rapid decrease of the c-Si fraction over a larger number of cycles for PSD_1 compared to PSD_2 (see Figure 3c).

In a full cell, all the Li in the cell is contained in the NMC cathode, and there is no Li metal foil to function as an “infinite” Li reservoir. As a result, the anode cannot be lithiated beyond the point reached in the very first cycle, as some Li will always be lost to electrolyte decomposition and/or Li trapping, and this is never replenished from a Li foil. Therefore, the amount of remaining c-Si was also determined at end-of-life (EoL) for a pouch cell using the powder with PSD_2. We defined EoL as the number of cycles achieved when the cell capacity reaches 80% of the initial capacity after formation (this corresponds to

cycle 5). The measurements were done at different locations across all three of the 6 x 4 cm electrodes, as shown in Figure 5.

This particular cell used a $\text{Li}(\text{Ni}_{0.83}\text{Mn}_{0.05}\text{Co}_{0.12})\text{O}_2$ cathode. After formation, the cell balance was ≈ 800 mAh g_{Si}⁻¹. However, because of the relatively high delithiation potential of Si, the first cycle CE at a lower cutoff of 3 V is relatively low; around 75% (not shown in the graph). Therefore, the lithiation depth in the first cycle was in fact close to that for half-cells at 1000–1100 mAh g_{Si}⁻¹.

Some variation is seen across the electrode area, as well as between the anode sheets, but the latter reflects the slight variation in balancing, and hence, Si utilization between the different anode/cathode pairs. The amount of remaining c-Si is consistently highest close to the tab, on all three anode layers. Point “B” has the most variation across different anodes, but points B, C, and D have approximately the same 3-layer average amount of c-Si remaining; roughly 44%.

The relative amount of remaining c-Si is only slightly lower than for the half-cell with PSD_2 cycled up to 100 cycles (Figure 3c), whereas the pouch cell was cycled nearly 200 cycles. The cross-sectioned partially lithiated electrode in Figure 1 showed lithiation to be quite homogeneous along every surface exposed to the electrolyte, so as long as the material does not fracture, no new c-Si would, in principle, get activated in a full cell. However, there is a significant amount of Li trapped in the Si anode, much more than in the half cells, as evidenced

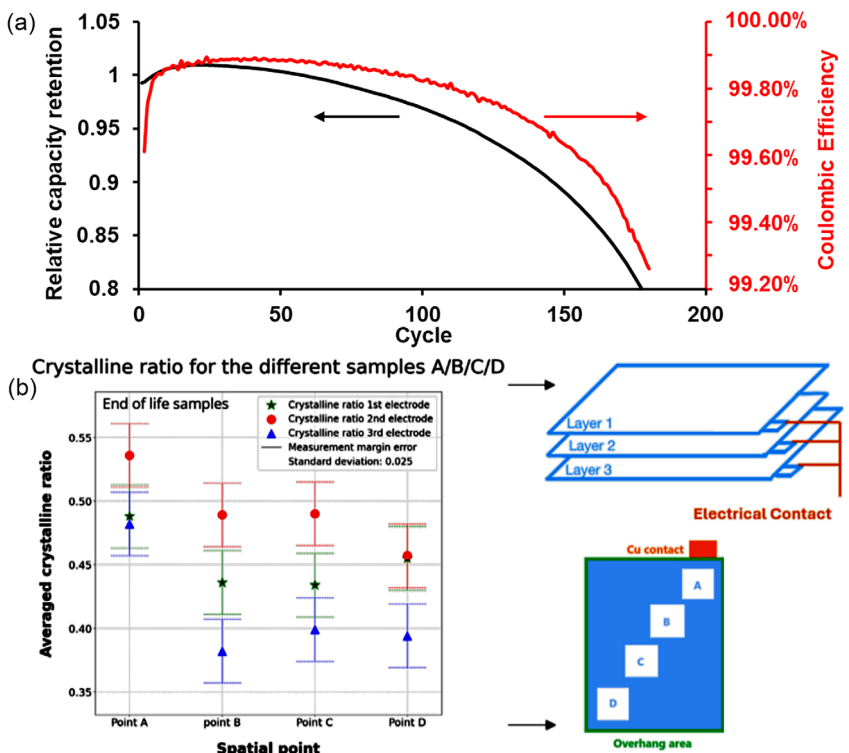


Figure 5. a) Capacity retention and CE versus cycle number (after formation) for a 3-layer pouch cell. b) Crystalline ratio for different locations (A, B, C, D) on the 3 anode foils at the EoL pouch cell.

by the much lower 1st CE in the full cell, and it is not known whether this trapped Li will slowly migrate into the c-Si backbone over time, which would also reduce the amount of c-Si measured with XRD. There is also some evidence from molecular dynamics simulations that Si atoms can be quite mobile at low Li concentrations, though this may mainly play a role on surfaces.^[29] When lithiation in a half-cell is limited to the exact amount delithiated in the previous cycle, which more closely resembles what happens in a full cell with a finite Li supply, the dQ/dV curves look more or less identical, as shown in Figure S5, Supporting Information. Operando XRD measurements could potentially shed more light on this (part of a future dedicated publication).

3.2. Electrode and Cell Expansion

One of the purposes of introducing porosity inside the Si particles is to mitigate outward expansion of the particles, and as a result, lessen the expansion of the anode and cell stack as a whole. The PSD_2 powder was reprocessed in a way that removed all the fines by using an elbow classifier, resulting in a powder with PSD_3 (see inset in Figure 6a). Practically speaking, the majority of particles in PSD_3 are large enough to accommodate internal porosity, as shown in Figure S6, Supporting Information. Therefore, PSD_3 can be regarded as a '100% porous' powder, as opposed to PSD_1 and _2 and is better representative of the effect of porosity w.r.t. a fully nonporous powder.

Figure 6a shows the PSDs of the all-porous PSD-3 and that of the same nonporous powder shown in Figure 2a and the main

panel shows the operando dilatometry curves for both. The nonporous powder expands considerably more at any lithiation depth and has approximately double the expansion of the PSD_3 powder at 2000 mAh g_{Si}⁻¹ (*t* = 44 h), once again emphasizing the expansion-inhibiting effect of the internal porosity.

Figure 6b shows the operando expansion curve of the silicon anode (blue curve) along with ex situ measurements performed as indicated (yellow dots and gray diamond). The operando measurement for PSD_3 shows that expansion is accelerating over the course of lithiation. At a lithiation depth of 500 mAh g_{Si}⁻¹, the relative expansion with regard to the initial thickness is 4.7%, at 1000 mAh g_{Si}⁻¹, the relative expansion is 16%. Between 1000 and 2000 mAh g_{Si}⁻¹, the relative expansion triples to 54%.

Figure 6c shows the half-cell data for the nonporous and PSD-3 powder. The PSD-3 powder has a higher 1st and maximum CE, and is also more stable than nonporous powder, consistent with its lower expansion.

For the ex situ measurements, lithiation was performed in half-cell configuration, after which the coin cell was decrimped and the working electrode recovered from the cell. The electrode thickness was measured using a digital micrometer, or a contact gauge, from Mitutoyo before and after lithiation. Six electrodes were averaged for each powder, and 3 points on each electrode were measured. The ex situ measurement shows a similar trend to the operando curve, where the measured expansion more than triples between 1000 and 2000 mAh g_{Si}⁻¹ from 22% to 68%. The ex situ measurements are consistently somewhat above the

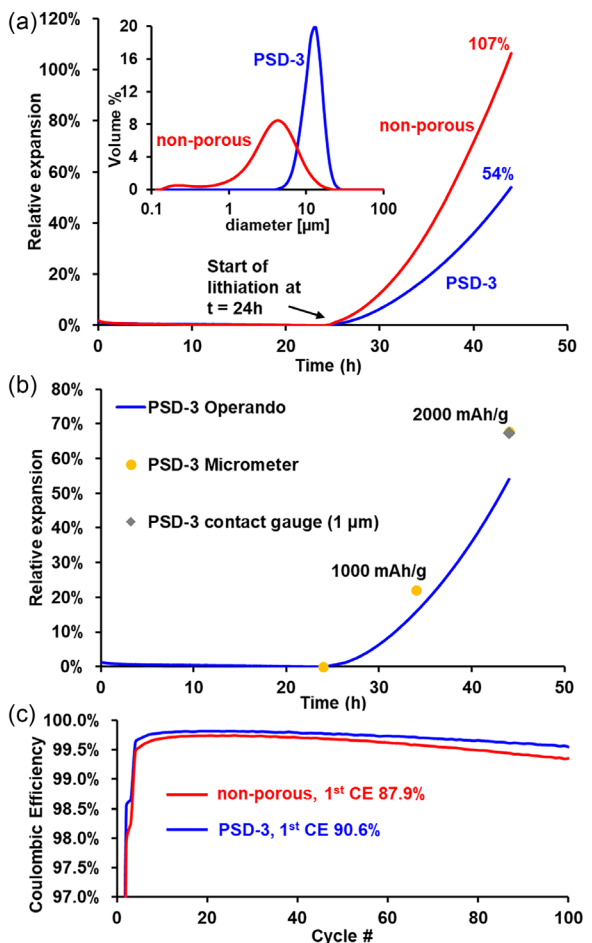


Figure 6. a) Operando dilatometry curves for a nonporous powder and the PSD_3 powder. The PSDs are shown in the inset. b) Relative expansion of the anode active layer for PSD_3 powder measured using three different methods: operando (blue curve), using an electronic micrometer (yellow dots), and using a contact gauge with a readability of 1 micron. The x-axis includes the 24 h resting period for the operando curve. c) Half-cell data for Coulombic Efficiency vs Cycle #.

operando measurements. The electrodes show a significant bend after extraction from the coin cells, particularly at $2000 \text{ mAh g}_{\text{Si}}^{-1}$, but this should not influence a thickness measurement using the micrometer, which has a flat area $\frac{1}{4}$ inch in diameter. The electrodes are not washed because additional swelling was observed after rinsing the electrodes, so residual electrolyte and salt simply dry up inside the electrode and are still present during the thickness measurements, which may inflate the value to a certain extent.

If we consider a (solid) particle level, the expected relative expansion would be $(2000/3578)*270\% = 151\%$. This linearization is justified, as the partial molar volume of Li inside Si is known to be practically constant.^[21] Of course, not all of that expansion would be directed upwards and the interparticle porosity inside the anode would also be expected to buffer some of the volume changes, in addition to the intraparticle porosity. A direct comparison between solid and porous particles using the same ex situ measurement methods is included in Figure S7, Supporting Information. The nonporous powder is a commercially

available product made by Elkem.^[30] The expansion of anodes prepared with nonporous powder is consistently larger than that of porous PSD_3 powder.

Operando dilatometry was also performed on a four-layer (four double-sided cathodes, three double-sided, and two single-sided anodes) pouch cell using a similar setup as in Ref. [27,31], but at a lower stack pressure of 2 bar. Anodes were prepared using PSD_2 (jet-milled) powder. As shown in Figure 7, the (reversible) relative volume change of the stack, including packaging, was slightly under 3.5% and the irreversible expansion was essentially zero. The cell was balanced with a NMC811 cathode to a Si utilization around $1000 \text{ mAh g}_{\text{Si}}^{-1}$ between 3 and 4 V. The thickness of the cathodes should barely change during cycling, as do the inactive components such as the Cu and Al current collectors and the pouch itself. A reversible expansion of 3.5% on the stack level is comparable to recent findings for Graphite/SiOx (22%) blends.^[31] It is considerably higher than the $<1\%$ found for a PSD_1 powder, but the influence of the inert parts of the stack was much higher in that case, and a higher stack pressure was used as well.^[27]

3.3. Full Cell Cycling Stability

For full cell cycle life testing in coin cells, NMC622 cathodes were used with a loading commensurate with a Si utilization of $\approx 1000 \text{ mAh g}_{\text{Si}}^{-1}$ in a voltage range between 3 and 4 V. In this cell configuration, “PSD_4” powder shows the best performance of all the porous powders described here and reaches well over 200 cycles, as shown in the top part of Figure 8. PSD_4 powder was produced by a short ball milling treatment of the etched flakes, followed by a sedimentation step in IPA to partially remove the fines (see Figure S8, Supporting Information). The capacity retention curves represent 3-cell averages and three different formulations are presented. All three formulations in Table 2 are the result of internal optimization efforts. Formulation_II, is the optimum formulation for PSD_2 jet-milled powder and evolved from Formulation_I. Formulation_III, using a combination of a carbon black from Cabot’s “LITX” series and SWCNTs as conductive additives, shows optimum performance for PSD_4, reaching 235 cycles on average before falling below 80% capacity after formation. Development efforts of the jet-milling process, which is considered more easily scalable than planetary ball milling, to consistently produce powder with optimal PSD are ongoing.

For a direct comparison with nonporous micron-sized Si, a powder with a comparable PSD was prepared. The “nonporous version” of the powder (PSD_4) was prepared from pure Si wafers cast with the same process as the porous materials. A comparison of PSDs of samples PSD_1 to _4 is presented in Figure S8, Supporting Information. The PSDs of porous and nonporous PSD_4 and the latter’s constituent powders, as measured with the same laser diffraction-based method, as well as ion-polished cross-sections of the pristine electrodes, are shown in Figure S9, Supporting Information. The capacity retention and CE are shown in the bottom part of Figure 8. The porous PSD_4 powder is clearly superior in both capacity retention and CE, particularly

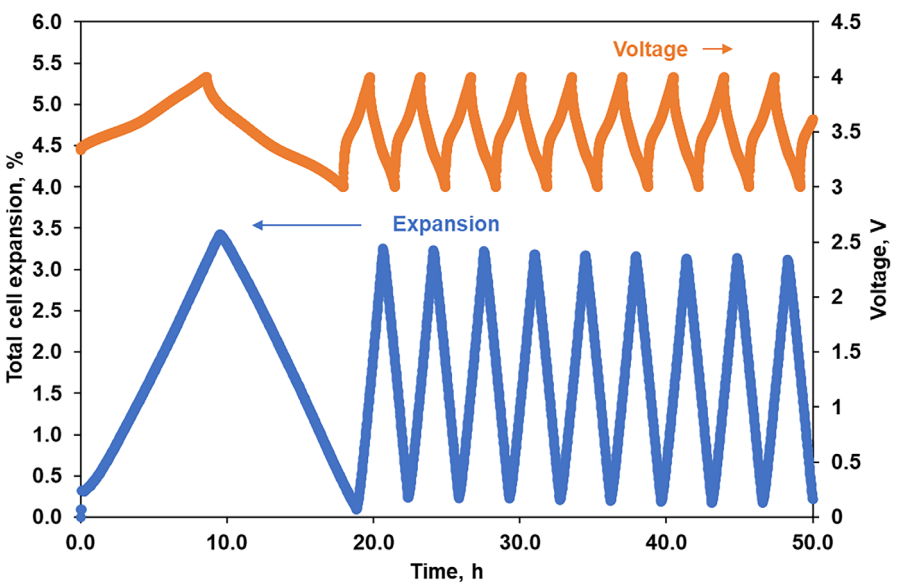


Figure 7. Operando dilatometry test performed in a multilayer pouch cell using PSD_2 powder. The energy density of the cell was $\approx 600 \text{ Wh l}^{-1}$ on stack level, that is, neglecting the pouch itself.

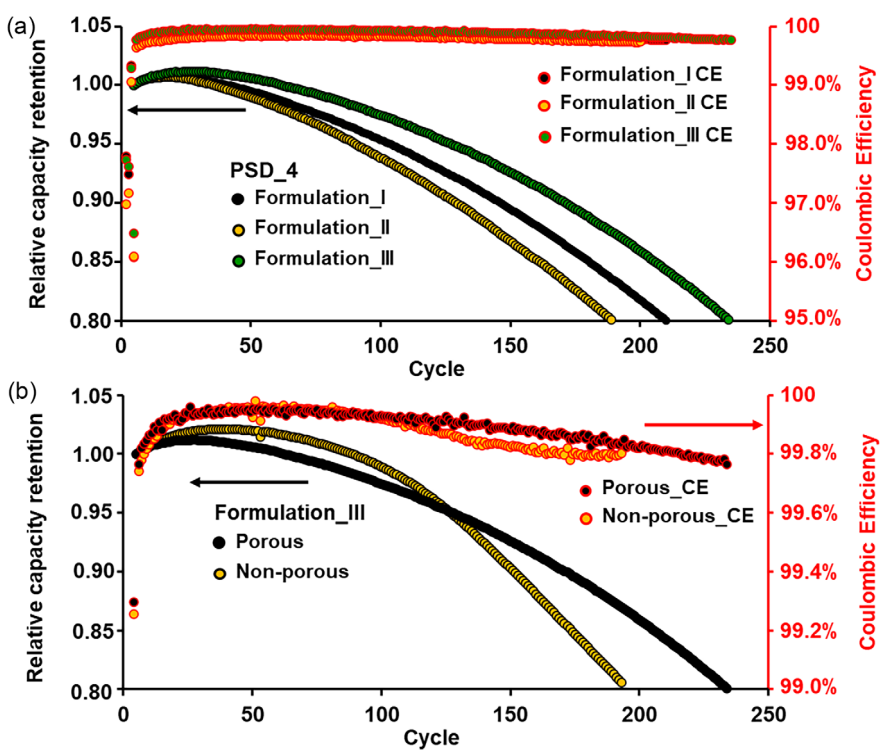


Figure 8. a) Capacity retention and CE for PSD_4 powder in three different formulations and b) comparison for porous PSD_4 and nonporous PSD_4 powder using Formulation_III (see Table 2).

after ≈ 100 cycles, compared to nonporous PSD_4. The silicon utilization for each sample is presented in Figure S10, Supporting Information.

The specific energy (stack level) of the cells presented in Figure 8 as well as the pouch cell from Figure 7 is $\approx 200 \text{ Wh kg}^{-1}$ at beginning of life. It should be kept in mind that these cells were

not optimized for energy density. The main point is the porous versus nonporous comparison of the active Si.

The original pore structure is maintained after cycling, as shown in Figure 9. No major cracks are observed within individual Si particles, even for quite large particles of $>10 \mu\text{m}$ diameter. Comparing the pristine and cycled electrodes, most of the

Table 2. Different anode formulations tested for PSD_4 (Figure S8, Supporting Information) powder.

	wt.%Si	wt.%CB	wt.%KS6	wt.%SWCNT	Ratio LiOH/PAA [g g^{-1}]	wt.%binder	first CE# [%]
Formulation_I	85	0.00	4.75	0.25	0.1	10	77.4
Formulation_II	85	2.45 SC45	2.45	0.10	0.2	10	76.5
Formulation_III	85	4.75 LITX-series	0.00	0.25	0.1	10	77.0

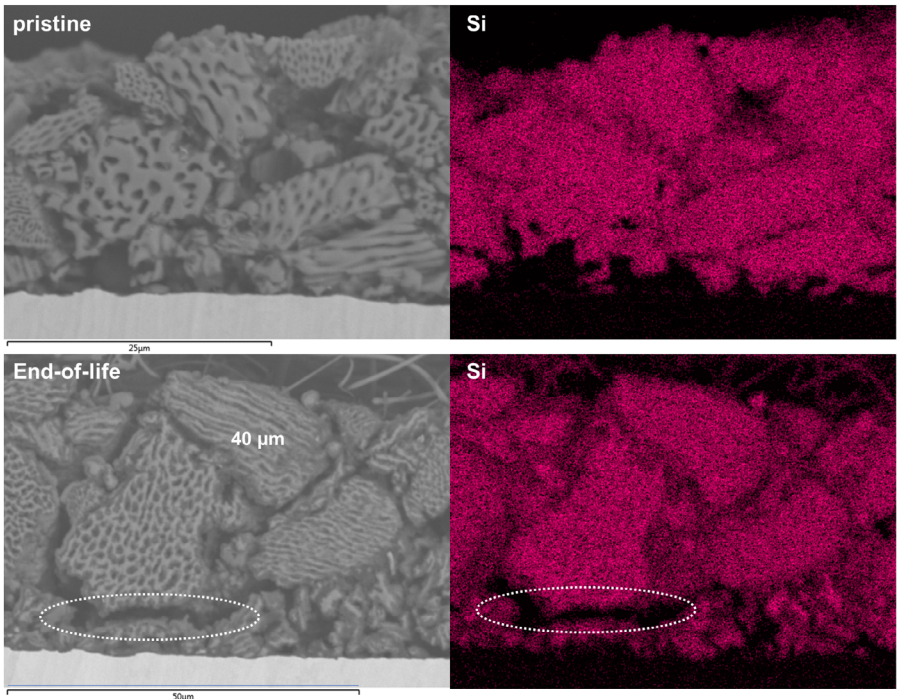


Figure 9. Ion-milled cross-sections of pristine and EoL electrodes with PSD_4 (porous) powder. Left: back-scattered electron images, right: Si EDX elemental mappings. The dotted line emphasizes a large crack that has formed during cycling.

capacity degradation appears to stem from electrolyte decomposition, rather than microstructural degradation of the Si itself, as there clearly is visible build-up of electrolyte decomposition products in the pores and around the Si particles. There is some degradation of the electrode structure itself as well, since the Si elemental mappings show the Si particles have drifted farther apart compared to the pristine state, further emphasized by the large void highlighted in the images. The images in Figure 9 were taken in back-scatter mode, which tends to emphasize the denser parts of the material. Secondary electron images included as Figure S11, Supporting Information, show the cycled electrode over a wider area and the structural degradation and solid electrolyte interphase (SEI) buildup are more clear there.

The Si-TM eutectic used here to produce porous Si has a high Si-content (85 at%) and the resulting porosity is relatively low (32%), in order to limit the SSA of the final powder. Although the cylindrical, parallel, but open, porosity in the material was effective at limiting expansion compared to nonporous material (see Figure 6), the internal surfaces in the pores do present additional surface area for SEI formation and loss of active Li. Closing the pores using encapsulation processes such as the one used by Chen et al. on a much higher porosity material from a Si-Al

eutectic (12 at% Si)^[12] could be a successful strategy to further improve capacity retention.

4. Conclusion

In conclusion, the presented porous E-magy Si material shows robust performance in coin and pouch cell configurations, at a utilization of around $1000 \text{ mAh g}_{\text{Si}}^{-1}$. The unique morphology with parallel cylindrical pores provides a lasting c-Si backbone, as shown by XRD, and the proposed reaction mechanism (involving inward expansion of Si into the internal porosity) was confirmed by SEM and Raman microscopy. The pore structure effectively buffers volume expansion. Operando dilatometry showed a major reduction of anode expansion from around 75% for solid nonporous Si to 16% for the porous Si material; % stack expansion in a multilayer pouch cell (fabricated with double-sided coated anodes and cathodes) was observed to be less than 4%.

The internal pore structure also imparts superior cycling performance with respect to nonporous Si powder with comparable PSD. The original pore structure was observed to be intact after

cycling over 200 cycles, and even particles in the 10–20 µm range show no visible cracks. The main degradation mechanism is found to be degradation of the electrode structure and electrolyte decomposition, rather than the active material itself.

E-magy silicon is a low-cost and a high-capacity alternative material for Li-ion battery anodes targeting next-generation battery technologies. By combining low SSA porous silicon with highly regular, parallel, internal pore structure, the first cycle CE is over 90% in half cell configuration. Moreover, the high-silicon anode's performance is also demonstrated in full-cell configuration, both in coin cells and multilayer pouch cells fabricated with state-of-the-art electrolytes and cathode materials, demonstrating compatibility with standard industrial practices.

Supporting Information

The authors have added additional Figures and table within the Supporting Information, from Figure S1 to Figure S11 and Table S1.

Acknowledgements

The authors would like to thank Erik Schuring at TNO Petten for outstanding support on SEM and ion-milling, as well as Dr. Marc Bruggeman, who supported the Raman analysis as well. The collaboration at the ThermoFisher Brno Technology Center is acknowledged for performing SEM on lithiated anodes. The authors also gratefully acknowledge support by Conrad Szczuka, a very fruitful collaboration with the operando dilatometry results obtained with the nanodilatometer EL CELL set-up. The experimental data used in this research were generated through access to the Joint Research Centre's (JRC) Battery Energy Storage Testing (BESTEST) laboratory in Petten, the Netherlands under the Framework for access to the Joint Research Centre physical Research Infrastructures of the European Commission (Silicon dominant anodes for lithium ion batteries SONATINA project, Research Infrastructure Access Agreement No. 36712/1. Any opinions, findings, and conclusions or recommendations expressed in this article are those of the authors and do not necessarily reflect those of the European Commission). Professors Charles Cornet, Antoine Letoublon, and the enthusiastic groups of students at the Institut National des Sciences Appliquées (INSA)-Rennes are acknowledged for a great multi-year collaboration on X-ray diffraction.

Conflict of Interest

The authors declare no conflict of interest.

Author Contributions

Vanesa Ruiz: conceptualization (supporting); methodology (supporting); project administration (lead); visualization (supporting);

writing—review and editing (supporting). **Akam Osmanpour:** methodology (supporting); software (supporting); writing—review and editing (supporting). **Jurgen Poen:** resources (supporting). **Kamran Tariq:** resources (supporting); writing—review and editing (supporting). **Willem Peter Kalisvaart:** data curation (lead); formal analysis (lead); methodology (equal); visualization (lead); writing—original draft (lead); writing—review and editing (equal).

Data Availability Statement

The data that support the findings of this study are available in the supplementary material of this article.

Keywords: anode expansion • in-operando characterization • metallurgical-grade silicon • nanoporosity • silicon-dominant

- [1] W. He, W. Xu, Z. Li, Z. Hu, J. Yang, G. Qin, W. Teng, T. Zhang, W. Zhang, Z. Sun, X. Yu, *Adv. Sci.* **2025**, *12*, 2407540.
- [2] D. Luo, Y. Lu, G. Zhu, J. Li, X. Liu, H. Zhang, *J. Energy Chem.* **2025**, *103*, 63.
- [3] S. D. Beattie, D. Larcher, M. Morcrette, B. Simon, J.-M. Tarascon, *J. Electrochem. Soc.* **2008**, *155*, A158.
- [4] Tesla 2020 Battery Day Transcript September 22', can be found under [https://www.rev.com/transcripts/tesla-2020-battery-day-transcript-september-22#:~:text=Transcript%20September%202022,Tesla%202020%20Battery%20Day%20Transcript%20September%202022](https://www.rev.com/transcripts/tesla-2020-battery-day-transcript-september-22#:~:text=Transcript%20September%202022,Tesla%202020%20Battery%20Day%20Transcript%20September%202022,Battery%20Day%20on%20September%202022), (accessed: 27 June 2025).
- [5] NCA/Gr+SiO cylindrical cell can be found under <https://www.murata.com/en-eu/products/batteries/cylindrical> (accessed: 27 June 2025).
- [6] T. Hölderle, D. Petz, V. Kochetov, V. Baran, A. Kriele, Z. Hegedüs, U. Lienert, M. Avdeev, P. Müller-Buschbaum, A. Senyshyn, *Energy Storage Mater.* **2025**, *75*, 042.
- [7] Zenlabs High Energy EV pouch cells can be found under <https://static1.squarespace.com/static/59dbcd906f4ca35190c9ae84/t/5cac327223d25a000188813b/1554788979381/EPS+Range.pdf> (accessed: 27 June 2025).
- [8] G. F. Pach, P. R. Adhikari, J. Quinn, C. Wang, A. Singh, A. Verma, A. Colclasure, J. H. Kim, G. Teeter, G. M. Veith, N. R. Neale, G. M. Carroll, *ACS Energ. Lett.* **2024**, *9*, 2492.
- [9] A. Magasinski, P. Dixon, B. Hertzberg, A. Kvit, J. Ayala, G. Yushin, *Nat. Mater.* **2010**, *9*, 353.
- [10] J. Xiao, Q. Li, Y. Bi, M. Cai, B. Dunn, T. Glossmann, J. Liu, T. Osaka, R. Sugiura, B. Wu, J. Yang, J.-G. Zhang, M. S. Whittingham, *Nat. Energy* **2020**, *5*, 561.
- [11] A. D. Pathak, U. K. Chanda, K. Samanta, A. Mandal, K. K. Sahu, S. Pati, *Electrochim. Acta* **2019**, *317*, 654.
- [12] Z. Chen, Y. Luo, D. Yang, Y. Hu, H. Hou, N. Koratkar, G. Zhou, W. Liu, *Mater. Today* **2025**, *86*, 74.
- [13] J. Entwistle, A. Rennie, S. Patwardhan, *J. Mater. Chem. A* **2018**, *6*, 344.
- [14] R. Song, J. Di, L. Lv, L. Yang, J. Luan, H. Yuan, J. Liu, W. Hu, C. Zhong, *ACS Appl. Mater. Interfaces* **2025**, *17*, 7849.
- [15] J. Liang, X. Li, Z. Hou, W. Zhang, Y. Zhu, Y. Qian, *ACS Nano* **2016**, *10*, 2295.
- [16] M. Liu, J. Liu, Y. Jia, C. Li, A. Zhang, R. Hu, J. Liu, C. Wang, L. Ma, L. Ouyang, *Nanomicro. Lett.* **2025**, *17*, 297.
- [17] J. Chen, X. Fan, Q. Li, H. Yang, M. R. Khoshi, Y. Xu, S. Hwang, L. Chen, X. Ji, C. Yang, H. He, E. Garfunkel, D. Su, O. Borodin, C. Wang, *Nat. Energy* **2020**, *5*, 386.
- [18] L. Gu, J. Han, M. Chen, W. Zhou, X. Wang, M. Xu, H. Lin, H. Liu, H. Chen, J. Chen, Q. Zhang, X. Han, *Energy Storage Mater.* **2022**, *52*, 547.
- [19] Coreshell Team (02/20/25) 'From Quartz To Next Gen Batteries: A Dive Into Metallurgical Silicon' can be found under <https://www.coreshell.com/post/from-quartz-to-next-gen-batteries-a-dive-into-metallurgical-silicon> (accessed: 29 June 2025).
- [20] M. N. Obrovac, V. L. Chevrier, *Chem. Rev.* **2014**, *114*, 444.

- [21] M. N. Obrovac, L. Christensen, D. B. Le, J. R. Dahn, *J. Electrochem. Soc.* **2007**, *154*, A849.
- [22] J. He, Y. Deng, J. Han, T. Xu, J. Qi, J. Li, Y. Zhang, Z. Zhao, Q. Li, J. Xiao, J. Zhang, D. Kong, W. Wei, S. Wu, Q.-H. Yang, *Nat. Commun.* **2025**, *16*, 4858.
- [23] A. G. Schönecker, *EP1754264: Method for the Production of Crystalline Silicon Foils*, European Patent Office (EPO) **2007**.
- [24] A. G. Schönecker, M. A. Spreafico, P.-Y. Pichon, P. A. F. Berneron, A. M. Groenland, *EP4323311: Nano-Structured Silicon Material and Manufacturing Method for use in Lithium Ion Based Secondary Batteries*, European Patent Office (EPO) **2024**.
- [25] "Elbow Jet Air Classifier Equipment" can be found under <https://elcanindustries.com/elbow-jet-air-classifier/> (accessed: 29 June 2025).
- [26] 'Electrochemical Dilatometer ECD-4-nano' can be found under <https://www.el-cell.com/products/test-cells/electrochemical-dilatometer/ecd-4-nano/> (accessed: 29 June 2025).
- [27] F. Maroni, M. Spreafico, A. Schönecker, M. Wohlfahrt-Mehrens, M. Marinaro, *J. Electrochem. Soc.* **2022**, *169*, 080506.
- [28] 'CleanConnect Sample Transfer System. Inert gas and vacuum sample transfer solution' can be found <https://assets.thermofisher.com/TFS-Assets/MSD/Datasheets/cleanconnect-datasheet-ds0378.pdf> (accessed: 29 June 2025).
- [29] C. E. L. Foss, M. K. Talkhoncheh, A. ø. Ulvestad, H. F. Andersen, P. E. Vullum, N. P. Wagner, K. Friestad, A. Y. Koposov, A. van Duin, J. P. Mæhlen, *J. Phys.Chem. Lett.* **2025**, *16*, 2238.
- [30] "What is silicon powder? can be found <https://www.elkem.com/products/silicon/silicon-powder-micronized-silicon/> (accessed: 29 June 2025).
- [31] O. von Kessel, A. Avdyli, D. Vrankovic, K. P.Kai, P. Birke, *J. Power Sources* **2024**, *610*, 582.

Manuscript received: July 29, 2025

Revised manuscript received: September 22, 2025

Version of record online:
